IEEE Access
Multidisciplinary ⋮ Rapid Review ⋮ Open Access Journal

Received 6 July 2024, accepted 15 July 2024, date of publication 18 July 2024, date of current version 15 August 2024.

Digital Object Identifier 10.1109/ACCESS.2024.3430491

RESEARCH ARTICLE

Minimal-Learning-Parameter Based Adaptive Neural Network With Fractional-Order Sliding Mode Control for Satellite Formation Flying

GUOGANG WANG[1], WANKAI YUAN[1], AND XIN WANG[2]
[1]School of Information and Control Engineering, Jilin Institute of Chemical Technology, Jilin 132022, China
[2]School of Petrochemical Technology, Jilin Institute of Chemical Technology, Jilin 132022, China

Corresponding author: Guogang Wang (wang_guo_g@sina.com)

This work was supported by the Ph.D. Start-Up Fund under Grant 222012312010.

ABSTRACT This paper introduces a novel neural network adaptive fractional-order sliding mode control strategy based on the minimal learning parameter method (MLPNN-FOSMC). This method aims to solve the problem of relative position control in satellite formation flying (SFF), especially in the presence of model uncertainties, external disturbances, input saturation, and unknown actuator gains. First, the mathematical model for satellite relative positioning is derived. Then, a fractional-order sliding mode controller is introduced and integrated with a radial basis function (RBF) neural network and the minimal learning parameter (MLP) strategy to compensate for errors caused by model uncertainties and external disturbances. At the same time, adaptive control is employed to mitigate the impact of unknown actuator gains on the system. To address the non-smooth input saturation nonlinearity problem, a new saturation function with the smoothing properties of the hyperbolic tangent function is introduced. The system's stability is ensured by employing the Lyapunov theorem. Finally, a comparative analysis with traditional sliding mode control (SMC) and neural network sliding mode control based on minimal learning parameter (MLPNN-SMC) highlights the superiority of the proposed method.

INDEX TERMS Neural network, fractional order sliding mode control, adaptive control, satellite formation flying (SFF), radial basis function (RBF), minimum learning parameter (MLP).

I. INTRODUCTION

Satellite formation flying technology, as a significant innovation in modern aerospace exploration and application, has emerged prominently in various fields such as resource exploration, environmental monitoring, meteorological observations, and high-precision 3D imaging. Compared with traditional single satellite operations, SFF employs efficient and close coordination among multiple satellites, significantly enhancing mission coverage, data processing efficiency, and the flexibility and reliability of task execution. The importance of this technological innovation in modern aerospace missions has been widely recognized, as emphasized in [1] and [2]. However, the highly nonlinear, closely coupled dynamic model of formation flight control, along with challenges such as parameter perturbations and external disturbances, significantly increases the complexity of control system design.

To effectively address these challenges, a series of advanced control strategies have been developed and applied by researchers, including robust control [3], [4], adaptive control [5], [6], sliding mode control (SMC) [7], [8], and optimal control [9], [10]. Among these, sliding mode control (SMC) is a powerful robust control scheme that has been widely used in various fields. SMC has become a focal point of research due to its excellent capability in suppressing internal

The associate editor coordinating the review of this manuscript and approving it for publication was Zhiguang Feng.

uncertainties and external disturbances. The core strategy of sliding mode control is to design a rapidly switching control law that guides the system states towards a predefined sliding surface and stabilizes them on it, ensuring precise control of the system states. However, in practical situations, adaptive control techniques are often used in conjunction with SMC, as adaptive sliding mode control (ASMC) combines the advantages of both adaptive control and sliding mode control. In [11], a finite-time adaptive terminal sliding mode control strategy was adopted, achieving precise formation control while effectively maintaining the stability of the internal structure.

In [12], the successful application of fast terminal sliding mode control technology in the rapid reconfiguration of satellite formations was demonstrated, showcasing its rapid response advantages. A comprehensive satellite attitude control scheme based on sliding mode control theory, utilizing Lorentz forces and magnetic torques, was proposed in [13], which confirmed the potential of adaptive sliding mode control in aerospace applications. Additionally, ASMC has been applied in other fields, such as trajectory tracking for robotic airships [14], [15], attitude adjustment for quadrotor UAVs [16], [17], and landing control for helicopters [18]. Integer-order sliding mode control is pertained to in [13], [14], [15], [16], [17], and [18]. However, ASMC can also be used for the control of fractional-order systems. In [19], an adaptive fractional-order SMC scheme with a fuzzy logic estimator was proposed for a class of uncertain linear continuous-time systems. Furthermore, in [20], an adaptive fractional-order sliding mode controller with a neural network was proposed for vibration dynamic mass testing of Z-axis MEMS gyroscopes. Compared to integer-order SMC, fractional-order SMC includes fractional-order terms in the sliding manifold, enhancing tracking performance and disturbance rejection capabilities. Despite the numerous advantages of fractional-order sliding mode control, its limitations in terms of convergence speed and dependency on disturbance information cannot be overlooked.

Neural network, with its powerful nonlinear model approximation capability and self-learning and adjustment ability, have shown great potential in improving system control accuracy and convergence speed. Neural network was utilized in [21] to perform online estimation of the system's nonlinear uncertainties and external disturbances, effectively implementing control strategy. In [22], an adaptive learning method based on the RBF neural network was employed for sliding mode control, effectively addressing a series of challenges encountered in grid-connected inverter control. A sliding mode controller that used the switching function as input and controlled with continuous RBF functions was designed in [23], significantly mitigating harmonic current issues caused by nonlinear loads and thus improving the overall system performance. Additionally, high efficiency in dealing with high uncertainties and nonlinearity in magnetic levitation systems was demonstrated in [24], achieving precise tracking control targets and providing excellent robustness. In [25], an output feedback control scheme based on a neural network adaptive state observer was proposed to compensate for system uncertainties and noise, significantly enhancing the tracking accuracy and anti-interference capability of DC motor systems. Furthermore, neural networks have been applied in the control of hydraulic manipulator systems [26]. Similarly, in the control design of dual-arm robotic manipulators [27], a sliding mode control scheme based on Lyapunov stability theory and the RBF neural network not only ensured the asymptotic stability of the system under sliding mode but also effectively eliminated system disturbances. However, the impact of input saturation was not considered.

Inspired by the aforementioned research, this paper proposes an innovative control method named MPLNN-FOSMC, aimed at addressing model uncertainties, external disturbances, input saturation and partial actuator failure in SFF. This algorithm integrates fractional-order sliding mode control (FSMC), adaptive control, neural network technology, and the minimal learning parameter method. The stability of the system is proven through the Lyapunov equation. The main contributions of this paper are summarized as follows:

(1) By replacing traditional neural network weight adjustment with minimal learning parameter, the computational burden of the system is significantly reduced, enhancing convergence speed and real-time performance.

(2) Increasing the degrees of freedom and flexibility of the system improves its adaptability and stability in dynamic responses.

(3) By integrating adaptive fractional-order sliding mode control, minimal learning parameters, and neural networks, the proposed approach effectively addresses model uncertainties, external disturbances, and input saturation issues, compensating for the disturbances affecting actuators and thereby further improving control accuracy and system robustness.

The structure of the remainder of this paper is as follows: Section II introduces fractional-order and the mathematical model for satellite relative motion. Section III presents the controller design and stability analysis. Section IV shows the comparative simulation results. Section V concludes the paper and discusses future research directions.

II. PRELIMINARY AND SYSTEM DESCRIPTION

A. PRELIMINARIES OF FRACTIONAL- ORDER

Fractional-order extends the traditional operations of differentiation and integration to include non-integer orders [28], [29]. Denoted by ${}_aD_t^\alpha$, the fractional-order operator encompasses both fractional-order derivatives and fractional-order integrals in a unified expression defined as

$$ {}_aD_t^\alpha = \begin{cases} \frac{d^\alpha}{dt^\alpha} & 1\alpha = 0 \\ \int_a^t (d\tau)^{-\alpha}\alpha & < 0 \end{cases} \tag{1}$$

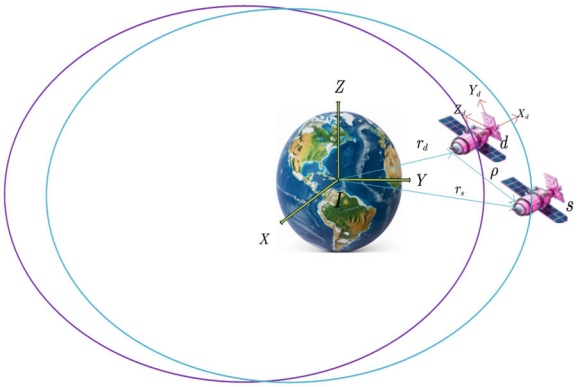

FIGURE 1. Diagram of satellite relative motion.

where a and t are the limits of the operator, and α is the fractional order of the operator. The operator is denoted by D^{α} for clarity in the following parts.

There are three commonly used definitions for general fractional-order operators: Grunwald–Letnikov (GL), Riemann–Letnikov (RL), and Caputo. Due to its stability and ease of use, the Caputo definition is more suitable for this system than the other two. Hence, we have chosen the Caputo. The αth Caputo derivative is defined as follows [28], [29]

$$D^{\alpha} f(t) = \frac{1}{\Gamma(1-\alpha)} \int_a^t (t-\tau)^{-\alpha} f(\tau)\, d\tau \tag{2}$$

where, $0 < \alpha < 1$, and $\Gamma(1-\alpha) = \int_0^{\infty} e^{-t} t^{-\alpha} dt$ is the Gamma function.

B. RELATIVE MOTION MODELING

Consider the two satellites depicted in Fig.1, which are orbiting the Earth. These satellites are referred to as the tracking satellite s (active satellite) and the target satellite d (passive satellite). To accurately describe their relative motion, two coordinate systems are introduced: Earth-Centered Inertial (ECI) and Local Vertical Local Horizontal (LVLH).

In the Earth-Centered Inertial (ECI) coordinate system, a coordinate system is established with the Earth at the origin and the equatorial plane as the reference. The X axis points towards the vernal equinox (a designated observation point on Earth), the Z axis is perpendicular to the equatorial plane and points towards the North Pole, and the Y axis completes the right-handed Cartesian coordinate system with the X and Z axes.

In the Local Vertical Local Horizontal (LVLH) coordinate system, the origin is set at the position of the target satellite, and a coordinate system is established that aligns with the satellite's motion. The X_d axis is defined to extend along the radial direction between the target and tracking satellites. The Z_d axis is perpendicular to the orbital plane and points in the direction of the satellite's angular momentum. Completing the right-handed Cartesian coordinate system, the Y_d axis is orthogonal to both the X_d and Z_d axes.

Under the influence of external disturbances, the relative motion equations of the two satellite with respect to the Earth-Centered Inertial coordinate system can be expressed as a set of equations.

$$\begin{cases} \ddot{\mathbf{r}}_{\mathbf{d}} = -\dfrac{\mu}{r_s^3}\mathbf{r}_{\mathbf{s}} \\ \ddot{\mathbf{r}}_{\mathbf{s}} = -\dfrac{\mu}{r_d^3}\mathbf{r}_{\mathbf{s}} + (\Delta\mathbf{d} + b\mathbf{u})/m_s \end{cases} \tag{3}$$

where r_s, r_d are the position vectors of the tracking satellite and the target satellite, respectively. $r_s = \|\mathbf{r}_{\mathbf{s}}\|$, $r_d = \|\mathbf{r}_{\mathbf{d}}\|$, $\mu = 398600\ \ \mathrm{km}^3/\mathrm{s}^2$. b is the actuator disturbance. $\Delta\mathbf{d}$ represent external disturbances and $\mathbf{u}$ represents the control torques.

To determine the relative motion between the tracking satellite and the target satellite, their relative position vector is defined as

$$\boldsymbol{\rho} = \mathbf{r}_{\mathbf{s}} - \mathbf{r}_{\mathbf{d}} \tag{4}$$

By substituting Eq. (4) into Eq. (3), the relative motion equation of the satellite in the Earth inertial coordinate system can be obtained

$$\ddot{\boldsymbol{\rho}} = -\frac{\mu}{\|\mathbf{r}_{\mathbf{d}} + \boldsymbol{\rho}\|^3}(\mathbf{r}_{\mathbf{d}} + \boldsymbol{\rho}) + \frac{\mu}{r_d^3}\mathbf{r}_{\mathbf{d}} + (\Delta\mathbf{d} + b\mathbf{u})/m_s \tag{5}$$

With the angular velocity of the orbital coordinate system relative to the Earth's inertial coordinate system being $\mathbf{w}$, $\ddot{\boldsymbol{\rho}}$ can be represented as

$$\ddot{\boldsymbol{\rho}} = \frac{\mathrm{d}^2\boldsymbol{\rho}}{\mathrm{d}t^2} + 2\mathbf{w} \times \frac{\mathrm{d}\boldsymbol{\rho}}{\mathrm{d}t} + \frac{\mathrm{d}\mathbf{w}}{\mathrm{d}t} \times \boldsymbol{\rho} + \mathbf{w} \times (\mathbf{w} \times \boldsymbol{\rho}) \tag{6}$$

Let $\boldsymbol{\rho} = [x\ y\ z]^{\mathrm{T}}$, The pursuing satellite and the target satellite can be represented in the orbital coordinate system as

$$\mathbf{r}_{\mathbf{s}} = \begin{bmatrix} r_d + x \\ y \\ z \end{bmatrix}, \mathbf{r}_{\mathbf{d}} = \begin{bmatrix} r_d \\ 0 \\ 0 \end{bmatrix} \tag{7}$$

where, $r_d = a\left(1-e^2\right)/(1+ecosv)$, v is true anomaly.

According to the Eqs. (3)-(7), the nonlinear differential equations describing the relative motion between satellite can be derived as follows [30], [31]

$$\begin{cases} \ddot{x} - w^2 x - \dot{w}^2 y - 2w\dot{y} - \mu/r_d^2 + \mu\left(r_d + x\right)/r_s^3 \\ \quad = bu_x/m_s + \Delta d_x \\ \ddot{y} + \dot{w}x - w^2 y + 2w\dot{x} + \mu y/r_s^3 = bu_y/m_s + \Delta d_y \\ \ddot{z} + \mu z/r_s^3 = bu_z/m_s + \Delta d_z \end{cases} \tag{8}$$

In the space environment, satellites are subject to various disturbances that significantly impact their motion, creating challenges for numerical analysis and implementation. To address these issues, the dynamics of satellites can be modeled as an interconnected system where forces are mutually coupled. For ease of calculation and practical application, a dynamic model can be constructed in the Local Vertical Local Horizontal (LVLH) coordinate system by separating

the terms that depend on satellite orbit information from other satellite-specific terms.

$$\begin{cases} \ddot{x} - w^2 x - \dot{w}^2 y - 2w\dot{y} - 2\mu x/r_d^3 - \Delta d_{cx} - \Delta d_x = bu_x/m_s \\ \ddot{y} + \dot{w}x - w^2 y + 2w\dot{x} + \mu y/r_d^3 - \Delta d_{cy} - \Delta d_y = bu_y/m_s \\ \ddot{z} + \mu z/r_d^3 - \Delta d_{cz} - \Delta d_z = bu_z/m_s \end{cases} \tag{9}$$

where

$$\Delta \mathbf{d_c} = \begin{bmatrix} \Delta d_{cx} \\ \Delta d_{cy} \\ \Delta d_{cz} \end{bmatrix} = \begin{bmatrix} \mu/r_d^2 - \mu\left(r_d + x\right)/r_s^3 - 2\mu x/r_d^3 \\ -\mu y/r_s^3 + \mu y/r_d^3 \\ -\mu z/r_s^3 - \mu z/r_d^3 \end{bmatrix}.$$

We define $\mathbf{d} = \Delta\mathbf{d}/m_s + \Delta\mathbf{d_c}$, u_i is the control acceleration.

A group of state variables are selected as $\mathbf{X} = [x\ \dot{x}\ y\ \dot{y}\ z\ \dot{z}]^T$ and $\dot{\mathbf{X}} = [\dot{x}\ \ddot{x}\ \dot{y}\ \ddot{y}\ \dot{z}\ \ddot{z}]^T$,then the relative motion dynamics of Eq. (9) can be transformed into the following forms

$$\dot{\mathbf{X}} = \mathbf{f} + \mathbf{d} + g\mathbf{u} \tag{10}$$

where, $g = b/m_s$ is the controller gain, $\mathbf{f} = \begin{pmatrix} l0 & 1 & 0 & 0 & 0 & 0 \\ w^2 + 2n_d^2 & \dot{w}^2 & 0 & 0 & -2w & 0 \\ 0 & 0 & 0 & 1 & 0 & 0 \\ -\dot{w} & w^2 - n_d^2 & 0 & -2w & 0 & 0 \\ 0 & 0 & 0 & 0 & 0 & 1 \\ 0 & 0 & -n_d^2 & 0 & 0 & 0 \end{pmatrix} \begin{bmatrix} x \\ \dot{x} \\ y \\ \dot{y} \\ z \\ \dot{z} \end{bmatrix}$ and $n_d^2 = \mu/r_d^3$.

Remark 1: When $0 < g < 1$, the actuator undergoes a partial loss of effectiveness, which results in reduced control authority. Conversely, when $g = 0$, the actuator suffers a complete loss of effectiveness, rendering it entirely nonfunctional. This paper primarily addresses the scenario of partial actuator failure, focusing on developing robust control strategies to maintain system performance despite the diminished actuator capability.

Due to the limitations of spacecraft engine thrust, it is necessary to consider the design of control commands u_i to ensure they comply with the saturation constraints. Therefore, a saturation formula has been established to describe this constraint, which is as follows

$$\text{sat}\left(u_i\right) = \begin{cases} \text{sgn}\left(u_i\right) u_{i,\max}, & \text{if } |\mathrm{u_i}| > \mathrm{u_{i,max}} \\ u_{i,}, & \text{if } |\mathrm{u_i}| \leqslant \mathrm{u_{i,max}}, \end{cases} \tag{11}$$

It is clear from equation (11) that the actual control signal $\text{sat}\left(u_i\right)$,being a piecewise-continuous function of u_i, exhibits nonsmoothed characteristic. This makes it difficult to implement in practical applications. To overcome this issue, we have developed a novel saturation nonlinearity function, described as follows

$$\begin{aligned} \text{sat}\left(u_i\right) = {} & u_{i,\max} \tanh\left(\frac{u_i}{u_{i,\max}}\right) \\ & + \left(1 - \tanh^2\left(\frac{u_i}{u_{i,\max}}\right)\right) \frac{u_i - u_{i,\max} \tanh\left(\frac{u_i}{u_{i,\max}}\right)}{u_i} \end{aligned} \tag{12}$$

Assumption 1: Both $\mathbf{d}$ and g are bounded, and they satisfy a condition wherein

$$\begin{cases} \varrho - \|\mathbf{d}\| > \varepsilon_M > \|\boldsymbol{\varepsilon}\| \\ 1 > g > 0 \end{cases} \tag{13}$$

where $\|\boldsymbol{\varepsilon}\|$ and ε_M are positive constants.

III. MPLNN -FOSMC CONTROLLER DESIGN

The objective of the tracking control problem in the system is to find a control law that enables the state trajectory $\mathbf{X}$ to track a desired reference trajectory $\mathbf{X_d}$. Assuming perfect knowledge of all system parameters, the design of an ideal fractional-order sliding mode controller for the system can be described step by step as follows:

Define the tracking error as

$$\mathbf{e} = \mathbf{X} - \mathbf{X_d} \tag{14}$$

The derivative of tracking error is

$$\dot{\mathbf{e}} = \dot{\mathbf{X}} - \dot{\mathbf{X}}_\mathbf{d} \tag{15}$$

The fractional-order sliding mode surface is designed as

$$\mathbf{s} = \lambda_1 \mathbf{e} + \lambda_2 \int \mathbf{e} dt + \lambda_3 D^{\alpha-1} \mathbf{e} \tag{16}$$

where λ_1, λ_2 and λ_3 are designed and adjustable parameters. $\alpha - 1$ is the fractional-order operation.

The derivative of the sliding surface is

$$\dot{\mathbf{s}} = \lambda_1 \dot{\mathbf{e}} + \lambda_2 \mathbf{e} + \lambda_3 D^\alpha \mathbf{e} \tag{17}$$

Substituting the Eqs. (14) and (15) into (17) and setting $\dot{\boldsymbol{s}} = 0$ yields

$$\begin{aligned} \dot{\mathbf{s}} &= \lambda_1 \dot{\mathbf{e}} + \lambda_2 \mathbf{e} + \lambda_3 D^\alpha \mathbf{e} \\ &= (\mathbf{f} + g\mathbf{u} + \mathbf{d} - \mathbf{X}_d) + \lambda_2 \mathbf{e} + \lambda_3 D^\alpha \mathbf{e} = \mathbf{0} \end{aligned} \tag{18}$$

The equivalent control force can be derived as

$$\mathbf{u_{eq}} = (\lambda_1 g)^{-1} \left(-\lambda_1 \mathbf{f} + \lambda_1 \mathbf{X_d} - \lambda_2 \mathbf{e} - \lambda_3 D^\alpha \mathbf{e}\right) \tag{19}$$

Since the control law

$$\begin{cases} \mathbf{u} = \mathbf{u_{eq}} + \mathbf{u_{sw}} \\ \mathbf{u_{sw}} = \lambda_1 \varrho \text{sgn}\left(\mathbf{s}\right) + \lambda_1 \rho \mathbf{s} \end{cases} \tag{20}$$

where ϱ, $\rho \in R^n$ denote the constant reaching coefficient and exponential reaching coefficient, respectively. $\text{sgn}\left(\mathbf{s}\right)$ is the signum function.

Then the proposed control can be designed as

$$\mathbf{u} = (\lambda_1 g)^{-1} (-\lambda_1 \mathbf{f} + \lambda_1 \mathbf{X_d} - \lambda_2 \mathbf{e} - \lambda_3 D^{\alpha} \mathbf{e} - \lambda_1 \varrho \mathrm{sgn}(\mathbf{s}) - \lambda_1 \rho \mathbf{s}) \tag{21}$$

Define a Lyapunov function candidate as

$$V_1 = \frac{1}{2} \mathbf{s}^{\mathrm{T}} \mathbf{s} \tag{22}$$

Substituting Eqs. (15) and (21) into the derivative of the Lyapunov function yields

$$\begin{aligned} \dot{V}_1 &= \mathbf{s}^{\mathrm{T}} \left[\lambda_1 (\mathbf{f} + g\mathbf{u} + \mathbf{d} - \mathbf{X_d}) + \lambda_2 \mathbf{e} + \lambda_3 D^{\alpha} \mathbf{e} \right] \\ &= \mathbf{s}^{\mathrm{T}} (\lambda_1 (\mathbf{d} - \varrho \mathrm{sgn}(\mathbf{s}) - \rho \mathbf{s})) \end{aligned} \tag{23}$$

Based on the assumption 1 and Lyapunov theorem, it is easy to prove that $\dot{V}_1 \leqslant 0$ and the system is global asymptotically stable.

In satellite formation flight control, while classical Radial Basis Function (RBF) networks can be utilized to approximate the uncertain terms between satellites, such algorithms do not perform optimally in meeting the demands of real-time control. To address this shortcoming, a minimum parameter learning method can be implemented to replace the weights within the existing neural network. This strategy, grounded in minimum parameter estimation, accelerates the convergence speed of the adaptive algorithm, thereby better conforming to the stringent real-time control requirements of satellite formation flight.

The RBFNN constructs dual mappings based on the input vector $\mathbf{X} = [X_1, X_2, \cdots, X_n]^{\mathrm{T}} \in \mathbf{R}^{\mathrm{n}}$ to the output $\hat{\mathbf{f}}(\mathbf{X})$.

$$\hat{\mathbf{f}}(\mathbf{X}) = \hat{\mathbf{W}}^{\mathrm{T}} \mathbf{h}(\mathbf{X}) \tag{24}$$

where, $\mathbf{W} \in \mathbf{R}^{\mathrm{p}}$ is the weight vector;p and n are the node number and input number, respectively;$\mathbf{h}(\mathbf{X}) = \left[h_1(\mathbf{X}), h_2(\mathbf{X}), \cdots, h_{\mathrm{p}}(\mathbf{X})\right] \in \mathbf{R}^{\mathrm{P}}$, A typical choice for $h_i(\mathbf{X})$ is a radial basis function.

$$\mathbf{h}_i(\mathbf{X}) = \exp\left(-\frac{\|\mathbf{X} - \mathbf{c_i}\|}{2\mathbf{b}_i^2}\right), i = 1, 2, \ldots, p \tag{25}$$

where, $\mathbf{c_i}$ is the center vector of the i-th hidden layer, and b_i is the width of the i-th hidden layer. The center of the hidden layer $\mathbf{c_i}$ and the width b_i are determined by the iterative algorithm adopted in [22]

$$\begin{cases} \Delta \mathbf{b}_i = (\mathbf{y} - \mathbf{y}_m) \mathbf{W}_i \mathbf{h}_i \dfrac{\|\mathbf{X} - \mathbf{c}\|^2}{\mathbf{b}_i^3} \\ \mathbf{b}_i(t) = \mathbf{b}_i(t-1) + \theta \Delta \mathbf{b}_j + \beta \left[\mathbf{b}_i(t-1) - \mathbf{b}_j(t-2)\right] \end{cases} \tag{26}$$

$$\begin{cases} \Delta \mathbf{b}_{ji} = (\mathbf{y} - \mathbf{y_m}) \mathbf{W}_i \dfrac{\mathbf{X}_i - \mathbf{c}_{ji}}{b_j^2} \\ \mathbf{c}_{ji}(t) = \mathbf{c}_{ji}(t-1) + \theta \Delta \mathbf{c}_{ji} + \beta \left[\mathbf{c}_{ji}(t-1) - \mathbf{c}_{ji}(t-2)\right] \end{cases} \tag{27}$$

where θ is the learning rate and β is the momentum factor.

For any continuous functions $\mathbf{f}(\mathbf{X})$, there exists an optimal weight vector $\mathbf{W}*$, such that

$$\mathbf{f}(\mathbf{X}) = \mathbf{W}^{*\mathrm{T}} \mathbf{h}(\mathbf{X}) + \boldsymbol{\varepsilon} \tag{28}$$

where, $\|\boldsymbol{\varepsilon}\| \leqslant \varepsilon_M$, and $\boldsymbol{\varepsilon}$ represents the approximation error.

Remark 2: We employ the Minimal Parameter Learning (MLP) method to approximate the function $\mathbf{f}(\mathbf{X})$. Let $\phi = \sup_{t>0} \|\mathbf{W}*(t)\|^2$ be a positive real number, where $\hat{\phi}$ represents the online estimation of ϕ, and the learning error is denoted as $\tilde{\phi} = \phi - \hat{\phi}$. This approach ensures that the minimal parameter learning can dynamically adjust to changes in the function's behavior over time, providing a robust method for real-time function approximation.

Remark 3: From Eq (24), $\mathbf{f}(\mathbf{X})$ is a six-dimensional unknown vector. Traditional neural networks, when estimating $\mathbf{f}(\mathbf{X})$ online, require six radial basis function (RBF) neural networks to update parameters simultaneously, significantly increasing the computational burden of the system. In contrast, we have adopted the minimal parameter learning method as shown in Remark 2, where only one neural network is needed to meet our requirements. This approach substantially reduces the computational load by simplifying the parameter update process. Additionally, the minimal learning parameter method can handle multi-dimensional outputs with a single network, enhancing efficiency and maintaining accuracy, making it a more practical choice for online estimation tasks.

The control law in Eq. (21) is redesigned as

$$\begin{aligned} \mathbf{u} = \left(\lambda_1 \hat{\mathbf{g}}\right)^{-1} \Bigg(&-\frac{1}{2} \lambda_1 \mathbf{s} \hat{\phi} \mathbf{h}^{\mathrm{T}}(\mathbf{X}) \mathbf{h}(\mathbf{X}) + \lambda_1 \mathbf{X_d} \\ &- \lambda_2 \mathbf{e} - \lambda_3 D^{\alpha} \mathbf{e} - \lambda_1 \varrho \mathrm{sgn}(\mathbf{s}) - \lambda_1 \rho \mathbf{s} \Bigg) \end{aligned} \tag{29}$$

Substituting the controller (29) into $\dot{\boldsymbol{s}}$, we can obtain equation as follows:

$$\begin{aligned} \dot{\boldsymbol{s}} &= \lambda_1 (\mathbf{f}(\mathbf{X}) + g\mathbf{u} + \mathbf{d} - \mathbf{X_d}) + \lambda_2 \mathbf{e} + \lambda_3 D^{\alpha} \mathbf{e} \\ &= \lambda_1 \hat{g} \frac{1}{\lambda_1 \hat{g}} \Bigg(-\frac{1}{2} \lambda_1 \mathbf{s} \hat{\phi} \mathbf{h}^{\mathrm{T}}(\mathbf{X}) \mathbf{h}(\mathbf{X}) + \lambda_1 \mathbf{X_d} - \lambda_2 \mathbf{e} \\ &\quad - \lambda_1 \rho \mathbf{s} - \lambda_3 D^{\alpha} \mathbf{e} - \lambda_1 \varrho \mathrm{sgn}(\mathbf{s}) \Big) + \lambda_1 \left(g - \hat{g}\right) \mathbf{u} \\ &\quad + \lambda_1 \mathbf{f}(\mathbf{X}) + \lambda_1 \mathbf{d} - \lambda_1 \mathbf{X_d} + \lambda_2 \mathbf{e} + \lambda_3 D^{\alpha} \mathbf{e} \\ &= -\frac{1}{2} \lambda_1 \mathbf{s} \hat{\phi} \mathbf{h}^{\mathrm{T}}(\mathbf{X}) \mathbf{h}(\mathbf{X}) + \lambda_1 \mathbf{X_d} - \lambda_2 \mathbf{e} - \lambda_3 D^{\alpha} \mathbf{e} \\ &\quad - \lambda_1 \varrho \mathrm{sgn}(\mathbf{s}) - \lambda_1 \rho \mathbf{s} + \lambda_1 \tilde{g} \mathbf{u} + \lambda_1 \mathbf{d} - \lambda_1 \mathbf{X_d} \\ &\quad + \lambda_2 \mathbf{e} + \lambda_3 D^{\alpha} \mathbf{e} + \lambda_1 \left(\mathbf{W}^{*\mathrm{T}} \mathbf{h}(\mathbf{X}) + \boldsymbol{\varepsilon}\right) \\ &= \lambda_1 \mathbf{W}^{*\mathrm{T}} \mathbf{h}(\mathbf{X}) + \lambda_1 (\boldsymbol{\varepsilon} + \mathbf{d}) - \frac{1}{2} \lambda_1 \mathbf{s} \hat{\phi} \mathbf{h}^{\mathrm{T}}(\mathbf{X}) \mathbf{h}(\mathbf{X}) \\ &\quad - \lambda_1 \varrho \mathrm{sgn}(\mathbf{s}) - \lambda_1 \rho \mathbf{s} + \lambda_1 \tilde{\mathbf{g}} \mathbf{u} \end{aligned} \tag{30}$$

According to the minimum parameter learning method and the adaptive law are designed as

$$\dot{\hat{\phi}} = \frac{\gamma_1}{2} \lambda_1 \mathbf{s}^{\mathrm{T}} \mathbf{s} \mathbf{h}^{\mathrm{T}}(\mathbf{X}) \mathbf{h}(\mathbf{X}) - \kappa_1 \gamma_1 \hat{\phi} \tag{31}$$

$$\dot{\hat{g}} = \gamma_2 \lambda_1 \mathbf{s}^{\mathrm{T}} \mathbf{u} - \kappa_2 \gamma_2 \hat{g} \tag{32}$$

where $\gamma_{1,2}$, $\kappa_{1,2}$ are positive constants.

Theorem 1: For the SFF nonlinear system with model uncertainties and external disturbances, as described by Equation (10), if the sliding surface is chosen according to Equation (16) and the MLPNN-FOSMC controller is designed according to Equation (30), where the dynamic uncertainties of the satellite are approximated by Equation (28) and the adaptation laws are given by Equations (31) and (32), then all signals of the closed-loop system are globally uniformly bounded and the position tracking error and angular velocity will asymptotically converge to zero.

Lemma 1: For the proof of system stability, the following derivations are necessitated.

$$\begin{aligned}\mathbf{s}^{\mathrm{T}}\mathbf{s}\phi\mathbf{h}^{\mathrm{T}}(\mathbf{X})\mathbf{h}(\mathbf{X})+1&=\|\mathbf{s}\|^2\left\|\mathbf{W}^*\right\|^2\mathbf{h}^{\mathrm{T}}(\mathbf{X})\mathbf{h}(\mathbf{X})+1\\&=\|\mathbf{s}\|^2\left\|\mathbf{W}^*\right\|^2\|\mathbf{h}(\mathbf{X})\|^2+1\\&\geqslant\|\mathbf{s}\|^2\left\|\mathbf{W}^{*\mathrm{T}}\mathbf{h}(\mathbf{X})\right\|^2+1\\&\geqslant 2\|\mathbf{s}\|\|\mathbf{W}^{*\mathrm{T}}\mathbf{h}(\mathbf{X})\|\end{aligned}$$

that is

$$\|\mathbf{s}\|\left\|\mathbf{W}^{*T}\mathbf{h}(\mathbf{X})\right\|\leqslant\frac{1}{2}\mathbf{s}^{\mathrm{T}}\mathbf{s}\phi\mathbf{h}^{\mathrm{T}}(\mathbf{X})\mathbf{h}(\mathbf{X})+\frac{1}{2}\tag{33}$$

Lemma 2: Due to $(\tilde{a}+a)^2\geqslant 0$, thus $\tilde{a}^2+2\tilde{a}a+a^2\geqslant 0$, that is

$$2\tilde{\phi}\hat{\phi}\geqslant\tilde{\phi}^2-\phi^2\tag{34}$$

$$2\tilde{g}\hat{g}\geqslant\tilde{g}^2-g^2\tag{35}$$

Proof. Select the following Lyapunov function candidate

$$V_2=\frac{1}{2}\mathbf{s}^{\mathrm{T}}\mathbf{s}+\frac{1}{2\gamma_1}\tilde{\phi}^2+\frac{1}{2\gamma_2}\tilde{g}^2\tag{36}$$

Differentiating Eq. (36) with respect to time, we obtain

$$\dot{V}_2=\mathbf{s}^{\mathrm{T}}\dot{\mathbf{s}}-\frac{1}{\gamma_1}\tilde{\phi}\dot{\hat{\phi}}-\frac{1}{\gamma_2}\tilde{g}\dot{\hat{g}}\tag{37}$$

According to Eq. (30), Eq. (37) can be rewritten as

$$\begin{aligned}\dot{V}_2&\leqslant\mathbf{s}^{\mathrm{T}}\Big[\lambda_1\mathbf{W}^{*\mathrm{T}}\mathbf{h}(\mathbf{X})+\lambda_1(\boldsymbol{\varepsilon}+\mathbf{d})-\lambda_1\rho\mathbf{s}\\&\quad-\frac{1}{2}\lambda_1\mathbf{s}\hat{\phi}\mathbf{h}^{\mathrm{T}}(\mathbf{X})\mathbf{h}(\mathbf{X})-\lambda_1\varrho\mathrm{sgn}(\mathbf{s})+\lambda_1\tilde{g}\mathbf{u}\Big]\\&\quad-\frac{1}{\gamma_1}\tilde{\phi}\dot{\hat{\phi}}-\frac{1}{\gamma_2}\tilde{g}\dot{\hat{g}}\\&\leqslant s^{\mathrm{T}}\left[\lambda_1\boldsymbol{\varepsilon}+\lambda_1\mathbf{d}-\lambda_1\rho\mathbf{s}-\lambda_1\varrho\mathrm{sgn}(\mathbf{s})\right.\\&\quad\left.+\lambda_1\tilde{g}\mathbf{u}-\frac{1}{2}\lambda_1\mathbf{s}\hat{\phi}\mathbf{h}^{\mathrm{T}}(\mathbf{X})\mathbf{h}(\mathbf{X})\right]\\&\quad+\lambda_1\|\mathbf{s}\|\left\|\mathbf{W}^{*\mathrm{T}}\mathbf{h}(\mathbf{X})\right\|-\frac{1}{\gamma_1}\tilde{\phi}\dot{\hat{\phi}}-\frac{1}{\gamma_2}\tilde{g}\dot{\hat{g}}\end{aligned}\tag{38}$$

From lemma 1, we obtain

$$\begin{aligned}\dot{V}_2&\leqslant\frac{1}{2}\lambda_1\mathbf{s}^{\mathrm{T}}\mathbf{s}\phi\mathbf{h}^{\mathrm{T}}(\mathbf{X})\mathbf{h}(\mathbf{X})+\frac{1}{2}\mathbf{s}^{\mathrm{T}}\lambda_1(\boldsymbol{\varepsilon}+\mathbf{d})+\frac{\lambda_1}{2}\\&\quad-\frac{1}{2}\lambda_1\mathbf{s}^{\mathrm{T}}\mathbf{s}\hat{\phi}\mathbf{h}^{\mathrm{T}}(\mathbf{X})\mathbf{h}(\mathbf{X})-\mathbf{s}^{\mathrm{T}}\lambda_1\varrho\mathrm{sgn}(\mathbf{s})\\&\quad-s^T\lambda_1\rho\mathbf{s}-\lambda_1\tilde{g}\mathbf{s}^{\mathrm{T}}\mathbf{u}-\frac{1}{\gamma_1}\tilde{\phi}\dot{\hat{\phi}}-\frac{1}{\gamma_2}\tilde{g}\dot{\hat{g}}\\&\leqslant\frac{1}{2}\lambda_1\mathbf{s}^{\mathrm{T}}\mathbf{s}\tilde{\phi}\mathbf{h}^{\mathrm{T}}(\mathbf{X})\mathbf{h}(\mathbf{X})+\lambda_1\mathbf{s}^{\mathrm{T}}(\varepsilon+\mathbf{d})+\lambda_1\tilde{g}\mathbf{s}^{\mathrm{T}}\mathbf{u}\\&\quad+\frac{1}{2}\lambda_1-\lambda_1\varrho\|\mathbf{s}\|-\lambda_1\mathbf{s}^{\mathrm{T}}\rho\mathbf{s}-\frac{1}{\gamma_1}\tilde{\phi}\dot{\hat{\phi}}-\frac{1}{\gamma_2}\tilde{g}\dot{\hat{g}}\end{aligned}\tag{39}$$

Lemma 3: [26] For $V:[0,\infty)\in R$, to solve inequality $\dot{V}<-aV+f,\forall t\geqslant t_0\geqslant 0$

$$V(t)\leqslant e^{-a(t-t_0)}V(0)+\int_{t_0}^{t}e^{-a(t-t_0)}f(\tau)\,d\tau\tag{40}$$

Due to, $\|\mathbf{s}\|\|\boldsymbol{\varepsilon}+\mathbf{d}\|\geqslant\mathbf{s}^T(\boldsymbol{\varepsilon}+\mathbf{d})$,Eq. (39) will become

$$\begin{aligned}\dot{V}_2&\leqslant\tilde{\phi}\left(\frac{1}{2}\lambda_1\mathbf{s}^{\mathrm{T}}\mathbf{s}\mathbf{h}^{\mathrm{T}}(\mathbf{X})\mathbf{h}(\mathbf{X})-\frac{1}{\gamma_1}\dot{\hat{\phi}}\right)+\frac{1}{2}\lambda_1-\lambda_1\mathbf{s}^T\rho\mathbf{s}\\&\quad+\tilde{g}\left(\lambda_1\mathbf{s}^T\mathbf{u}-\frac{1}{\gamma_2}\dot{\hat{g}}\right)+\lambda_1\|\mathbf{s}\|\|\boldsymbol{\varepsilon}+\mathbf{d}\|-\lambda_1\varrho\|\mathbf{s}\|\end{aligned}\tag{41}$$

By choosing $\varrho\geqslant\varepsilon_M+\|\mathbf{d}\|$, the $\dot{V}_2$ can be rewritten as follows:

$$\begin{aligned}\dot{V}_2&\leqslant\tilde{\phi}\left(\frac{1}{2}\lambda_1\mathbf{s}^{\mathrm{T}}\mathbf{s}\mathbf{h}^{\mathrm{T}}(\mathbf{X})\mathbf{h}(\mathbf{X})-\frac{1}{\gamma_1}\dot{\hat{\phi}}\right)\\&\quad+\tilde{g}\left(\lambda_1\mathbf{s}^T\mathbf{u}-\frac{1}{\gamma_2}\dot{\hat{g}}\right)+\frac{1}{2}\lambda_1-\lambda_1\mathbf{s}^{\mathrm{T}}\rho\mathbf{s}\end{aligned}\tag{42}$$

Substituting adaptive laws (31) and (32) into Eq. (42), it yields

$$\begin{aligned}\dot{V}_2&\leqslant-\kappa_1\tilde{\phi}\hat{\phi}+\frac{1}{2}\lambda_1-\kappa_2\tilde{g}\hat{g}-\lambda_1\rho\mathbf{s}^{\mathrm{T}}\mathbf{s}\\&\leqslant-\frac{\kappa_1}{2}\left(\tilde{\phi}^2-\phi^2\right)-\frac{\kappa_2}{2}\left(\tilde{g}^2-g^2\right)+\frac{1}{2}\lambda_1-\lambda_1\mathbf{s}^{\mathrm{T}}\rho\mathbf{s}\\&=-\frac{\kappa_1}{2}\tilde{\phi}^2-\frac{\kappa_2}{2}\tilde{g}^2-\lambda_1\mathbf{s}^{\mathrm{T}}\rho\mathbf{s}+\frac{\kappa_1}{2}\phi^2+\frac{\kappa_2}{2}g^2+\frac{1}{2}\lambda_1\end{aligned}\tag{43}$$

From lemma 2, it can be obtained.

$$\begin{aligned}\dot{V}_2&\leqslant-\frac{\kappa_1\gamma_1}{2\gamma_1}\tilde{\phi}^2-\frac{\kappa_2\gamma_2}{2\gamma_2}\tilde{g}^2-\lambda_1\rho\mathbf{s}^{\mathrm{T}}\mathbf{s}+\frac{\kappa_1}{2}\phi^2+\frac{\kappa_2}{2}g^2+\frac{1}{2}\lambda_1\\&\leqslant-\frac{\kappa_1\gamma_1}{2\gamma_1}\tilde{\phi}^2-\frac{\kappa_2\gamma_2}{2\gamma_2}\tilde{g}^2-\frac{2\lambda_1\rho\mathbf{s}^{\mathrm{T}}\mathbf{s}}{2}+\frac{\kappa_1}{2}\phi^2\\&\quad+\frac{\kappa_2}{2}g^2+\frac{1}{2}\lambda_1\\&\leqslant-2\Lambda V_2+R\end{aligned}\tag{44}$$

where, $\Lambda=\min(\kappa_1\gamma_1,\kappa_2\gamma_2,2\lambda_1\rho)$, $R=\frac{\kappa_1}{2}\phi^2+\frac{\kappa_2}{2}g^2+\frac{1}{2}\lambda_1$.

From lemma 3, the information can be obtained as follows:

$$V_2(t)\leqslant\left(V_2(0)-\frac{\Lambda}{R}\right)\exp(-\Lambda t)+\frac{\Lambda}{R}\tag{45}$$

Thus, $V_2=\lim_{t\to\infty}V_2(t)=\frac{\Lambda}{R}$,which implies that

$$\|\mathbf{s}\|\leqslant\sqrt{2\left(V_2(0)-\frac{\Lambda}{R}\right)\exp(-\Lambda t)+\frac{\Lambda}{R}}\tag{46}$$

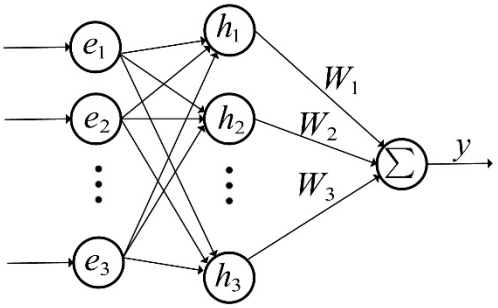

FIGURE 2. The structure of RBF neural network.

From Eqs (44)-(46), it can be seen that $s, e, \tilde{\phi}$ and $\tilde{g}$ are all bounded, implying that all signals are bounded. This completes the proof.

Remark 4: Due to the presence of the discontinuous function sgn (**s**) in the control law (29), the discontinuous control input can lead to chattering phenomena. To mitigate the occurrence of chattering, we replace the discontinuous function with a continuous one. Specifically, sgn (**s**) is replaced with sgn (**s**) $= \frac{\mathbf{s}}{\mathbf{s}+\Phi}$, where Φ is a small positive parameter.

IV. SIMULATION RESULTS

In the current section, simulation results and corresponding discussions are presented to demonstrate the effectiveness and robustness of the designed controllers. i The components of the expected trajectory along the x_d, y_d and z_d axes are $x_d = 40 * \cos(10t)$, $y_d = 40 * \cos(11t)$ and $z_d = 40 * \cos(12t)$, respectively. In Eq. (16), the sliding parameters are chosen as $\lambda_1 = 1, \lambda_2 = 1.3, \lambda_3 = 5$. Φ is selected as 0.01.

The initial values of ϕ and g are 0.1, the initial value of **c** is always chosen between -1 and $+1$, we choose $\mathbf{c} = \begin{bmatrix} -0.1639 & 0.7487 & 0.5359 \\ -0.39 & -0.97 & 0.9717 \end{bmatrix}$ and $\mathbf{b} = \begin{bmatrix} 0.2 & 0.2 & 0.2 \end{bmatrix}^T$. In (27), The gain coefficients are $\beta = 0.3, \theta = 0.2$ and in (30) $\gamma_1 = 30, \kappa_1 = 0.1, \gamma_2 = 1.2, \kappa_2 = 0.2$. At the same time, We choose the coefficient for the exponential convergence rate ρ and the switching gain coefficient in sliding mode control ϱ.

When $g = 1$, the simulation results are shown in Figures 3 to 8.

Figures 3 and 4 respectively show the tracking performance and stability accuracy of the three controllers, indicating that they can all enable the actual trajectory to follow the desired trajectory within a limited time. However, the new method stabilizes the system in just 1.8 seconds, while traditional SMC and MLPNN-SMC require 9.89 seconds and 7.09 seconds, respectively. The significantly improved convergence speed is also accompanied by enhanced steady-state accuracy.

Additionally, as shown in Figure 5, the controller's velocity error enhances the stability of formation flying, reducing the need for frequent position adjustments due to velocity errors and improving system performance. As shown in Figure 6,

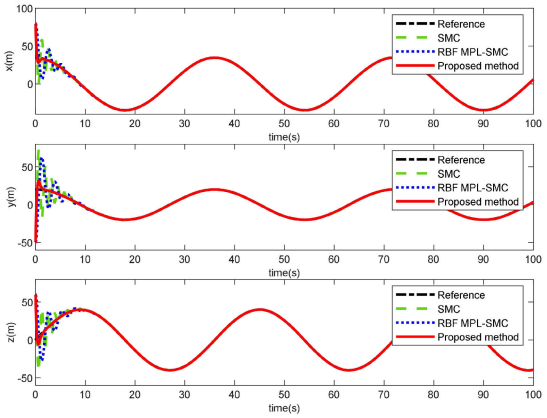

FIGURE 3. Property of the trajectory tracking.

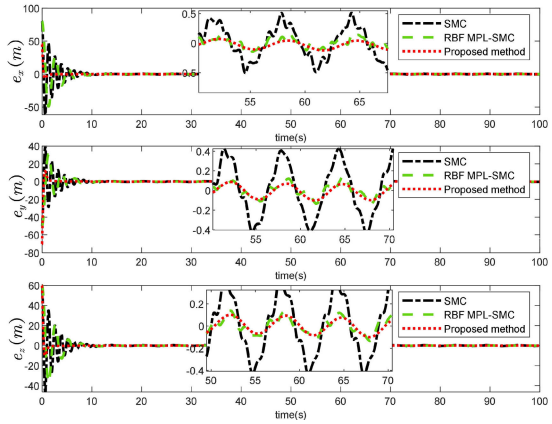

FIGURE 4. Property of the position tracking error.

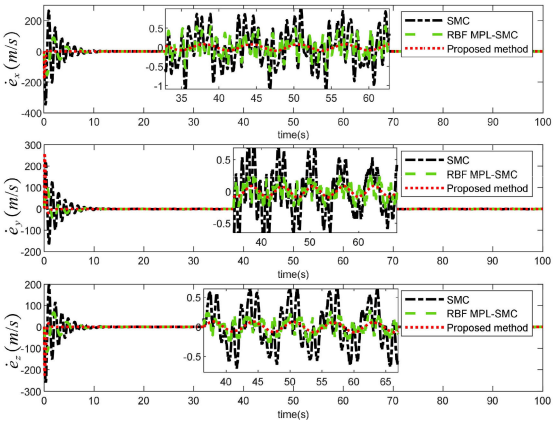

FIGURE 5. Property of the velocity tracking error.

the historical fluctuations of the sliding surface indicate that the new control method significantly reduces oscillations after stabilization. Figure 7 shows that, compared to SMC and MLPNN-SMC, the new method can stabilize the control force more quickly, reducing excessive oscillations and improving system operational efficiency.

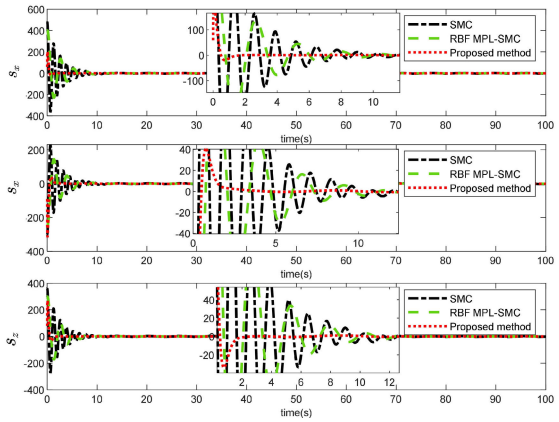

FIGURE 6. Property of the sliding surface.

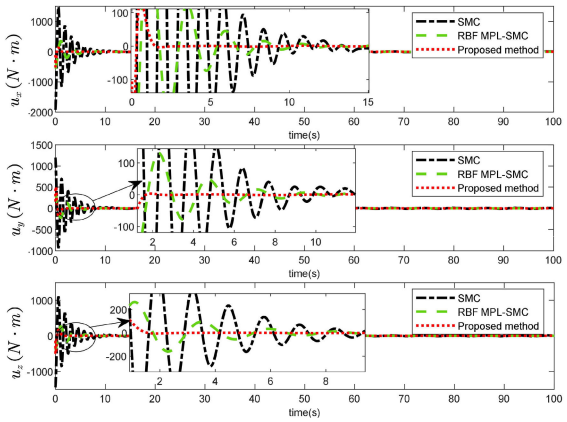

FIGURE 7. Control torques.

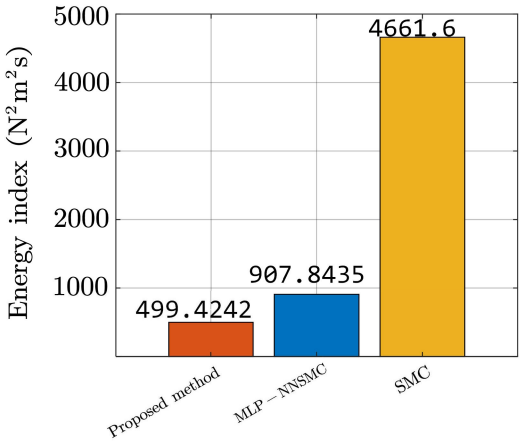

FIGURE 8. Energy consumption.

Lastly, Fig 8 presents a comparative analysis of the energy consumption by the three control schemes, assessed via the energy metric function $E = \int_{t_0}^{t_f} \sum_{i=1}^{3} |\mathbf{u}_i(t)| dt$. It is discernibly evident from Fig 8 that, relative to SMC and MLPNN-SMC,

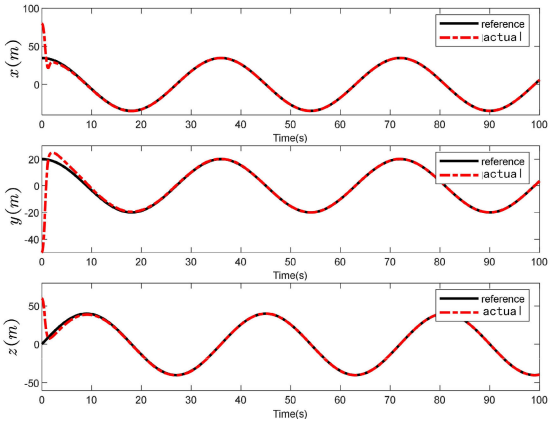

FIGURE 9. Property of the trajectory tracking.

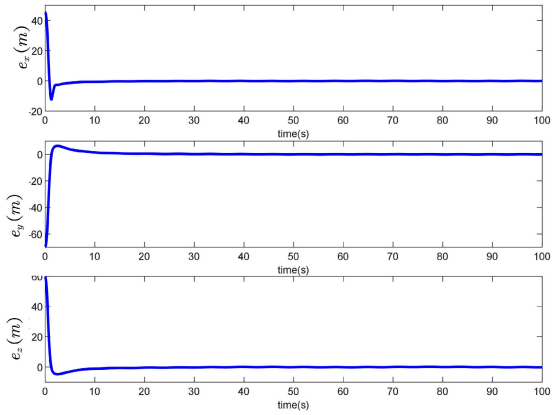

FIGURE 10. Property of the position tracking error.

the novel approach incurs significantly lower energy consumption.

When $g = 0.6 + 0.4\exp(-0.2t)$ and the saturation limit is 150 N · m,this means that the actuator is constrained and cannot reach its maximum expected output. The simulation results are shown in Figures 9 to 14.

Figures 9 and 10 show the tracking curves and their errors, indicating that the system remains stable even when the actuators lose partial effectiveness and are subject to saturation limits. Figure 11 presents the historical fluctuations of the sliding surface, demonstrating that the sliding surface can stabilize near the zero region within a finite time. Figure 12 shows that the control torques are successfully constrained within the range of 150 N · m.

Figure 13 indicates that $\hat{g}$ and $\hat{\phi}$ are both bounded. Figure 14 illustrates that in the xyz -plane, the actual trajectory can fully track the desired trajectory. These results indicate that, as stated in Theorem 1, all signals in the closed-loop tracking control system of SFF are bounded. Therefore, the proposed neural network adaptive fractional-order sliding mode control scheme with minimal learning parameter is effective for tracking SFF under the influence of model uncertainties, external disturbances, input saturation, and partial actuator failures.

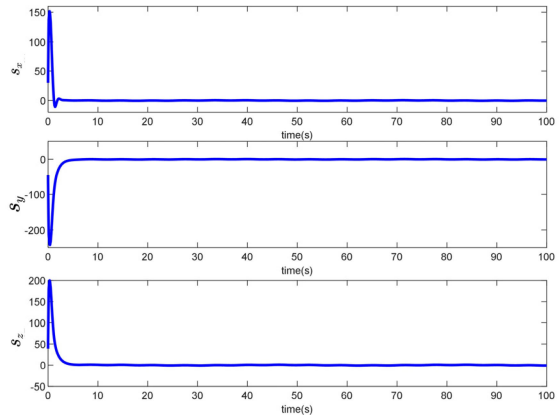

FIGURE 11. Property of the sliding surface.

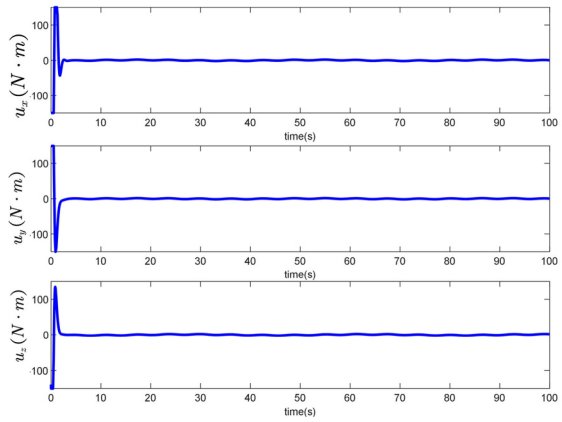

FIGURE 12. Control torques.

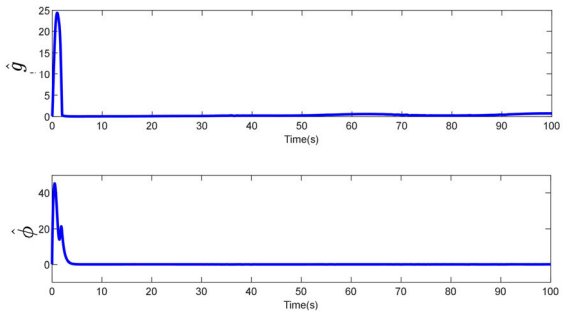

FIGURE 13. The estimations of ϕ and φ.

Remark 5: (1) The proposed MLPNN-FOSMC controller exhibits efficiency and robustness in controlling the relative position of satellites, capable of handling model uncertainties, external disturbances, input saturation, and partial actuator failures. (2) The designed MLPNN approximator can effectively estimate the upper bounds of the total uncertainties of the satellite online and compensate for the impact of uncertainties. (3) Compared to SMC controllers and MLPNN-SMC, the MLPNN-FOSMC controller provides higher precision and effectively reduces chattering,

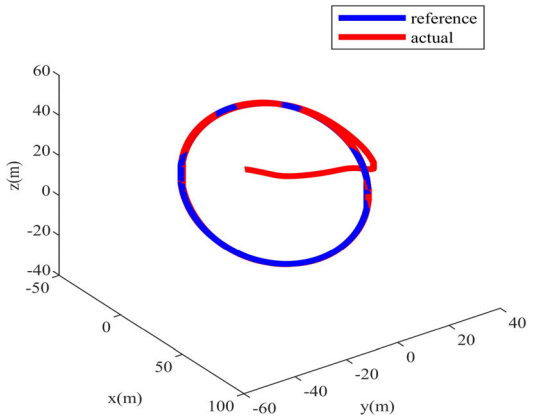

FIGURE 14. Reference and actual trajectories in the xyz-plane.

demonstrating its advanced and practical capabilities in the field of aerospace relative position control.

V. CONCLUSION

This paper proposes an innovative neural network adaptive fractional-order sliding mode control strategy to address the problem of relative position control in satellite formation flying, characterized by model uncertainties, external disturbances, input saturation, and unknown actuator gains. By integrating fractional-order sliding mode control, neural networks, and minimal parameter learning, this method meets real-time requirements and effectively handles model uncertainties and external disturbances. Additionally, adaptive control is employed to manage unknown actuator gains, and the introduction of a smooth saturation function successfully addresses the issue of non-smooth input saturation nonlinearity. Using the proposed control scheme, all signals of the closed-loop system are uniformly bounded, achieving relative position control in satellite formation flying. Future research should include expanding the event-triggering mechanism under limited communication resources and investigating prescribed performance control to meet specific performance criteria within a predetermined time.

REFERENCES

[1] R. Kristiansen and P. J. Nicklasson, "Spacecraft formation flying: A review and new results on state feedback control," *Acta Astronautica*, vol. 65, nos. 11–12, pp. 1537–1552, Dec. 2009.

[2] C. T. Fraser and S. Ulrich, "Adaptive extended Kalman filtering strategies for spacecraft formation relative navigation," *Acta Astronautica*, vol. 178, pp. 700–721, Jan. 2021.

[3] S. M. Joshi, A. G. Kelkar, and J. T.-Y. Wen, "Robust attitude stabilization of spacecraft using nonlinear quaternion feedback," *IEEE Trans. Autom. Control*, vol. 40, no. 10, pp. 1800–1803, Sep. 1995.

[4] C. Liu, Z. Sun, K. Shi, and F. Wang, "Robust dynamic output feedback control for attitude stabilization of spacecraft with nonlinear perturbations," *Aerosp. Sci. Technol.*, vol. 64, pp. 102–121, May 2017.

[5] D. Thakur, S. Srikant, and M. R. Akella, "Adaptive attitude-tracking control of spacecraft with uncertain time-varying inertia parameters," *J. Guid., Control, Dyn.*, vol. 38, no. 1, pp. 41–52, Jan. 2015.

[6] K. W. Lee and S. N. Singh, "Noncertainty-equivalence adaptive attitude control of satellite orbiting around an asteroid," *Acta Astronautica*, vol. 161, pp. 24–39, Aug. 2019.

[7] K. Lu, Y. Xia, Z. Zhu, and M. V. Basin, "Sliding mode attitude tracking of rigid spacecraft with disturbances," *J. Franklin Inst.*, vol. 349, no. 2, pp. 413–440, Mar. 2012.
[8] Q. Li, L. Liu, Y. Deng, S. Tang, and Y. Zhao, "Twistor-based synchronous sliding mode control of spacecraft attitude and position," *Chin. J. Aeronaut.*, vol. 31, no. 5, pp. 1153–1164, May 2018.
[9] Y. Park, "Robust and optimal attitude stabilization of spacecraft with external disturbances," *Aerosp. Sci. Technol.*, vol. 9, no. 3, pp. 253–259, Apr. 2005.
[10] J. Yao, Q. Hu, and J. Zheng, "Nonlinear optimal attitude control of spacecraft using novel state-dependent coefficient parameterizations," *Aerosp. Sci. Technol.*, vol. 112, May 2021, Art. no. 106586.
[11] M. Alipour, M. Malekzadeh, and A. Ariaei, "Practical fractional-order nonsingular terminal sliding mode control of spacecraft," *ISA Trans.*, vol. 128, pp. 162–173, Sep. 2022.
[12] C. Zhang, J. Wang, D. Zhang, and X. Shao, "Synchronization and tracking of multi-spacecraft formation attitude control using adaptive sliding mode," *Asian J. Control*, vol. 21, no. 2, pp. 832–846, Mar. 2019.
[13] X. Huang and Y. Yan, "Fully actuated spacecraft attitude control via the hybrid magnetocoulombic and magnetic torques," *J. Guid., Control, Dyn.*, vol. 40, no. 12, pp. 3358–3360, Dec. 2017.
[14] Y. Yang and Y. Yan, "Trajectory tracking for robotic airships using sliding mode control based on neural network approximation and fuzzy gain scheduling," *Proc. Inst. Mech. Eng., I, J. Syst. Control Eng.*, vol. 230, no. 2, pp. 184–196, Feb. 2016.
[15] Y. Yang, "A time-specified nonsingular terminal sliding mode control approach for trajectory tracking of robotic airships," *Nonlinear Dyn.*, vol. 92, no. 3, pp. 1359–1367, May 2018.
[16] H. Razmi and S. Afshinfar, "Neural network-based adaptive sliding mode control design for position and attitude control of a quadrotor UAV," *Aerosp. Sci. Technol.*, vol. 91, pp. 12–27, Aug. 2019.
[17] Y. Yang and Y. Yan, "Attitude regulation for unmanned quadrotors using adaptive fuzzy gain-scheduling sliding mode control," *Aerosp. Sci. Technol.*, vol. 54, pp. 208–217, Jul. 2016.
[18] Y. Huang, M. Zhu, Z. Zheng, and M. Feroskhan, "Fixed-time autonomous shipboard landing control of a helicopter with external disturbances," *Aerosp. Sci. Technol.*, vol. 84, pp. 18–30, Jan. 2019.
[19] M. Qian, Y. Shi, Z. Gao, and X. Zhang, "Integrated fault tolerant tracking control for rigid spacecraft using fractional order sliding mode technique," *J. Franklin Inst.*, vol. 357, no. 15, pp. 10557–10583, Oct. 2020.
[20] J. Fei and C. Lu, "Adaptive fractional order sliding mode controller with neural estimator," *J. Franklin Inst.*, vol. 355, no. 5, pp. 2369–2391, Mar. 2018.
[21] H. Feng, Q. Song, S. Ma, W. Ma, C. Yin, D. Cao, and H. Yu, "A new adaptive sliding mode controller based on the RBF neural network for an electro-hydraulic servo system," *ISA Trans.*, vol. 129, pp. 472–484, Oct. 2022.
[22] D. Wu, B. Long, and Y. Cheng, "RBF-NN based upper-bound adaptive learning sliding mode control for grid-connected converter," in *Proc. IEEE Int. Conf. Mechatronics Autom. (ICMA)*, Oct. 2020, pp. 960–965.
[23] J. Fei, Z. Wang, X. Lu, and L. Deng, "Adaptive RBF neural network control based on sliding mode controller for active power filter," in *Proc. 32nd Chin. Control Conf.*, 2013, pp. 3288–3293.
[24] X. Su, Y. Xu, and X. Yang, "Neural network adaptive sliding mode control without overestimation for a Maglev system," *Mech. Syst. Signal Process.*, vol. 168, Apr. 2022, Art. no. 108661.
[25] X. Yang, W. Deng, and J. Yao, "Neural network based output feedback control for DC motors with asymptotic stability," *Mech. Syst. Signal Process.*, vol. 164, Feb. 2022, Art. no. 108288.
[26] X. Yang, W. Deng, and J. Yao, "Neural adaptive dynamic surface asymptotic tracking control of hydraulic manipulators with guaranteed transient performance," *IEEE Trans. Neural Netw. Learn. Syst.*, vol. 34, no. 10, pp. 7339–7349, Oct. 2023.
[27] A. Yadav, A. Kumar, and B. Bhushan, "Sliding mode control with RBF neural network for two link robot manipulator," *Int. J. Comput. Appl.*, vol. 178, no. 52, pp. 31–36, Sep. 2019.
[28] S. Dadras and H. R. Momeni, "Fractional terminal sliding mode control design for a class of dynamical systems with uncertainty," *Commun. Nonlinear Sci. Numer. Simul.*, vol. 17, no. 1, pp. 367–377, Jan. 2012.
[29] A. Sharafian, A. Sharifi, and W. Zhang, "Fractional sliding mode based on RBF neural network observer: Application to HIV infection mathematical model," *Comput. Math. Appl.*, vol. 79, no. 11, pp. 3179–3188, Jun. 2020.
[30] Q. He and C. Han, "Dynamics and control of satellite formation flying based on relative orbit elements," in *Proc. AIAA Guid., Navigat. Control Conf. Exhibit*, Aug. 2008.
[31] H. D. Curtis, "Preliminary orbit determination," in *Orbital Mechanics for Engineering Students*, 3rd ed., H. D. Curtis, Ed., Boston, MA, USA: Butterworth-Heinemann, 2014, Ch. 5, pp. 239–298.

GUOGANG WANG received the master's and Ph.D. degrees from Changchun University of Technology, China.

He is currently a Lecturer and a Graduate Advisor with Jilin Institute of Chemical Technology, China. His research interests include robotics control and spacecraft control.

WANKAI YUAN received the B.S. degree from Liaoning University of Petroleum and Chemical Technology, China, in 2020. He is currently pursuing the master's degree with Jilin Institute of Chemical Technology, China.

His research interests include neural networks, sliding-mode control, and spacecraft attitude and orbit coupling control.

XIN WANG received the master's degree from Hefei University of Technology, China, and the Ph.D. degree from Changchun University of Technology, China.

She is currently a Lecturer and a Graduate Advisor with Jilin Institute of Chemical Technology, China. Her research interests include the green preparation technologies of functional materials and the extraction of natural products.